# STATISTICAL ANALYSIS OF GRAINS AND PORES WITHIN POLYCRYSTALLINE $AL_2TIO_5$ CERAMICS, BASED ON X-RAY COMPUTED TOMOGRAPHY

PHILIPP RIEDER[1*], LUKAS PETRICH[1], ITZIAR SERRANO-MUNOZ[2], MOSSAAB MOUIYA[3,4] , HENNING MARKÖTTER[2] MARC HUGER[3], GIOVANNI BRUNO[2], VOLKER SCHMIDT[1]

Abstract. Advanced statistical image analysis workflows were developed to segment and quantitatively evaluate 2D electron-backscatter diffraction (EBSD) maps and 3D synchrotron X-ray computed tomography (SXCT) volumes of a polycrystalline $Al_2TiO_5$ refractory composite that contains microcracks and pores. Several size, shape, and further geometric descriptors were determined for both the solid phase ($Al_2OTi_5$ grains) and the pore space. The resulting pore-size distribution is distinctly bimodal: coarse pores (tens to hundreds of micrometers), traced to incomplete powder compaction, coexist with fine pores generated during sintering. The two pore populations appear to be correlated with grain growth and crystallographic orientation in different ways. Finally, the descriptors obtained from the 2D EBSD and 3D SXCT data sets are internally consistent but complementary, highlighting the value of characterizations based on EBSD and SXCT in the microstructural study of refractory ceramics.

*Keywords.* Synchrotron X-ray computed tomography; electron-backscatter diffraction; aluminum titanate; morphological reconstruction; segmentation; statistical image analysis

## 1. Introduction

Ceramics are typically characterized as rigid, strong, yet brittle materials. Overcoming this brittleness could broaden their range of applications and enhance their performance in existing uses [1–3]. Flexible ceramics hold potential for various applications, including antivibration materials and refractory components with improved resistance to thermal shocks. Due to its high thermal expansion anisotropy, which induces microcracking and consequently flexibility [4], aluminum titanate (AT) has gained increasing attention as an engineering ceramic in various fields [5–9], making it a particularly intriguing material. According to Bayer [10], the thermal expansion coefficients along its crystallographic directions are $\alpha a = -2.9 \times 10^{-6} K^{-1}, \alpha b = 10.3 \times 10^{-6} K^{-1}$ and $\alpha c = 20.1 \times 10^{-6} K^{-1}$. The inherent low strength of AT is attributed to this anisotropy, as it leads to significant microcracking during cooling from the sintering temperature. These microcracks are predominantly formed at the grain interfaces because of mismatches in the thermal expansion coefficients, causing differential shrinkage under temperature variations and generating stress at the grain boundaries. Consequently, microcrack behavior can be controlled by designing specific microstructures (e.g., grain size and shape) to generate a customized network of microcracks [11].

[1]Institute of Stochastics, Ulm University, Helmholtzstraße 18, 89069 Ulm, Germany
[2]Bundesanstalt für Materialforschung und -prüfung, Unter den Eichen 87, 12200 Berlin, Germany
[3] Université Limoges, Institut de Recherche sur les Céramiques, UMR CNRS 7315, 12 Rue Atlantis, 87000 Limoges, France
[4]University Mohammed VI Polytechnic (UM6P), Materials Science, Energy and Nanoengineering Department, Lot 660, Hay Moulay Rachid, 43150 Ben Guerir, Morocco

In this context, microstructural features need to be characterized in detail to reliably elucidate the relationship between microstructure and microcraking behavior. Typically, the characterization of such microstructural features is performed by means of 2D microscopy (see, e.g., [12]). However, 2D image analysis provides limited information about morphological properties such as grain size and shape, while 3D image analysis enables more accurate determinations of such quantities. Specifically, synchrotron X-ray computed tomography (SXCT) offers unparalleled insights into the 3D internal structure of materials [13, 14]. A key advantage of SXCT over other imaging techniques is its non-destructive nature, making it particularly valuable for analyzing delicate samples that cannot be easily sectioned or polished for microscopy. Additionally, SXCT data can be quantitatively analyzed, virtually sliced in any direction, or digitally modified - such as colorcoding specific components — to enhance visualization of the 3D morphology.

But, in addition to costs and availability of 3D imaging techniques, the segmentation of complex 3D morphologies presents a greater challenge compared to 2D image data. Provided there is sufficient resolution and contrast, neural networks have proven to be a powerful tool to achieve good phase segmentations [15–17]. However, object-wise segmentations still rely on classical approaches, such as marker-based watershed transform, which is typically prone to oversegmentation of objects which are not spherical. To avoid oversegmentation, various methods have been proposed for thinning markers, such as the approaches in [18, 19], which are based on the extension of regional minimums or the so-called morphological reconstruction [20, 21]. Still, these approaches fail for a broad range of object geometries within one data set, as seen in the present application, where strongly elongated grains over a wide range of grain sizes lead to a simultaneous over- and undersegmentation.

In the present paper, in order to address this issue, a novel iterative segmentation approach is introduced for granular materials, utilizing the iterative application of morphological reconstruction. At each iteration, objects that fulfill a certain convexity criterion are accepted based on the assumption that the true grain shape is relatively convex. The resulting segmentation is then employed to determine several pore and grain descriptors, allowing a comprehensive statistical analysis. Specifically, bivariate probability densities are determined to establish correlations between size and shape descriptors of individual pores and grains, as well as further geometric descriptors of the materials considered in this paper.

## 2. Materials and methods

2.1. **Polycrystalline aluminum titanate.** $Al_2TiO_5$(AT) crystal grains exhibit pronounced anisotropy in their coefficient of thermal expansion (CTE). This feature makes AT-based materials an excellent model system for designing simplified microcracked refractory ceramics [22]. Simplifying refractory formulations to a limited number of components, compared to conventional industrial products, is particularly advantageous, as it allows a more precise analysis of key microstructural parameters (such as grain size, grain coarsening, and microcrack networks) and their influence on the thermomechanical properties, which are crucial for refractory materials. To explore these aspects, polycrystalline AT-based materials were synthesized on site (at IRCER) using a fine atomized powder (TM-20P) supplied by Marusu Company (Japan) [23]. The processing involved natural sintering in air under different thermal cycles, which varied in dwell time, followed by natural cooling to room temperature (see Table 1). These different thermal treatments produced two grades of material with different average grain sizes and varying degrees of microstructural damage that intend to mimic the microstructure of itacolumite, a very specific natural mineral consisting mainly of quartz that exhibits great flexibility [24].

These grades are designated as AT-F (flexible), characterized by a moderate grain size, and AT-VF (very flexible), which exhibits large grains.

| Reference | AT-F | AT-VF |
|---|---|---|
| Temperature | 1600°C | 1600°C |
| Dwell time | 2h | 8h |
| Apparent density | 3.21 g/cm$^3$ | 3.16 g/cm$^3$ |
| Porosity | 90.4% | 89.1% |
| Total pores volume fraction | 9.6% | 10.9% |
| Open pores volume fraction | 8.3% | 9.1% |
| Microcracks volume fraction | 3.7% | 3.9% |
| Total porosity excluding microcracks | 5.9% | 7.0% |

TABLE 1. Sintering conditions and resulting porosity for AT-F and AT-VF. The values were taken from [12].

The results presented in Table 1, adapted from [12], indicate that AT-F samples exhibit a higher porosity of 90.4%, while AT-VF samples show a slightly lower porosity of 89.1%. In the case of AT-VF samples, this notable reduction in relative density is attributed to a more extensive network of microcracks, as evidenced by the SEM images (see Figure 4 in [12]). This interpretation is further supported by the evolution of the open pore volume fraction, which accounts for microcrack-induced voids (9.1%). 2D EBSD images (see Figure 6 in [12]) clearly reveal that as the dwell time increases from 2h (F) to 8h (VF), the proportion of small grains decreases while the larger grains become dominant. Under the sintering conditions corresponding to the AT-F sample (1600°C for 2 hours), grain growth remains below 40 µm, while the sintering conditions of the AT-VF sample (1600°C for 8 hours) result in strongly elongated grains with sizes ranging from 7 µm to 100 µm.

The following sections focus on a statistical analysis of the AT-VF material, since the resolution of SXCT ($\approx 1.4$ µm) is sufficient to capture even the smaller grains contained in this sample. In contrast, a significant proportion of the grains of the AT-F material are at or below the resolution of the SXCT reconstructions, making a detailed analysis unreliable. For the sake of brevity, we will therefore present the methodology and the results for the AT-VF sample only.

2.2. **Synchrotron X-ray computed tomography (SXCT).** The SXCT experiments were carried out at the BAMline [25, 26] at BESSY II in Berlin, Germany. BAMline features hard X-rays, allowing for several applications [27]. The aluminum ceramics shown are recorded with a voxel size of 0.72 µm. During a 180° rotation, 2400 projections were recorded with an exposure time of 400 ms each. The field of view was $1.8 \times 1.5\,\mathrm{mm}^2$. A monochromatic X-ray beam at an energy of 25 keV, set by the W/Si double multilayer monochromator, was employed, resulting in an energy resolution $\Delta$ E/E of 3-4%. For image acquisition, a sCMOS PCO.edge 5.5 camera with $2560 \times 2160$ pixel was paired with a 60 µm thick CdWO4 scintillator screen. In total, each SXCT acquisition took approximately 16 minutes. The projection data was reconstructed with internal Python code based on the tomopy package [28] using grid-rec algorithm [29]. The derived 3D reconstruction was cropped so that only the AT material (that is, no air) is included within the analyzed volume. The resulting image is of size 686.88 µm × 730.08 µm × 223.92 µm ($\widehat{=}954 \times 1014 \times 311$ voxels with a voxel size of 0.72 µm). An exemplary 2D cross section of a 3D reconstructed volume is displayed in Figure 1a.

Lastly, a stripe-shaped artifact (due to the multilayer monochromator installed at the BAM-line) was manually identified and removed. The missing data was reconstructed using an in-painting method, implemented in the scikit-image package [30].

2.3. **EBSD measurements and segmentation.** The preparation of electron backscatter diffraction (EBSD) samples involved embedding the samples in a low-viscosity epoxy resin (IP, Presi France), which was made by mixing 5g of powder with 1ml of liquid hardener. This mixture is then poured over the samples placed in a plastic mold and placed in a vacuum chamber (approximately 1 kPa) for 1 hour. The impregnation efficiency depends on the ability of the rasin to penetrate into the open microcrack network. After curing for 12 hours in ambient air, a polishing step was performed on a Minitech 233 machine (Presi, France) following the protocol described in detail in [12].

The AT materials were examined using an environmental scanning electron microscope (FEI ESEM Quanta 450 FEG) with an electron dispersive spectroscopy (EDS) detector for chemical analysis. The microscope was operated at an accelerating voltage of 15 kV. The samples were observed in low vacuum mode without any conductive coating. All micrographs presented in this paper were captured in backscattered electron (BSE) contrast.

EBSD involved directing a focused electron beam at the surface of the sample and measuring the diffraction patterns generated as the electrons interact with the atomic lattice. This technique was performed using a ZEISS SUPRA 40VP scanning electron microscope equipped with a field emission gun, operating at an accelerating voltage of 20 kV. The scan size (ranging from $750 \times 750\,\mu m^2$ to $1800 \times 1800\,\mu m^2$) and the step size (from 0.5 to 1.0 µm) were customized to collect enough data for statistically representative analysis of each sample. This image acquisition procedure resulted in a pixel size of 1 µm. Data processing was performed utilizing the MTEX 5.11.2 [31] software package for MATLAB [32]. A grain was defined as consisting of at least 10 pixels with a misorientation less than 5° among them. Subsequently, to smooth the grains, a spline filter implemented in MTEX was applied. To interpolate missing EBSD data, grain-wise morphological closing [33] with a disk-shaped structuring element of radius $r = 2$ pixels was performed. Note that in each step of this segmentation procedure, grains consisting of less than 10 pixels ($\widehat{=}10\,\mu m^2$) were removed.

2.4. **SXCT image segmentation.** To statistically analyze the three phases – pore space, AT grains, and silica – individual pores and grains have to be identified. In Section 2.4.1 the segmentation of the three phases is pointed out, followed by an object-wise segmentation of individual pores and grains in Sections 2.4.2 and 2.4.3, respectively.

2.4.1. **Phase-wise segmentation.** For the phase-wise segmentation of the reconstructed 3D SXCT volume $I\colon W \mapsto [0, 255]$, the commercial software Dragonfly 2024.1 [34] was utilized, where $W = \{1, \dots, 954\} \times \{1, \dots, 1014\} \times \{1, \dots, 311\}$ denotes the three-dimensional sampling window. More precisely, a 3D U-net of depth 4, patch size of $32 \times 32 \times 32$ and an initial filter count of 32, which utilizes batch normalization, was used. It was trained on several hand-labeled cutouts of $I$. The neural network segmented $I$ into three binary images $I_{P^*}, I_{G^*}, I_{S^*}\colon W \mapsto \{0, 1\}$, corresponding to the pore phase, the AT phase, and the silica phase, respectively. The pore phase image $I_{P^*}$ is given by

$$I_{P^*}(x) = \begin{cases} 1, & \text{if } x \text{ corresponds to the pore phase,} \\ 0, & \text{else,} \end{cases}$$

for each $x \in W$. The AT phase $I_{\mathrm{G}^*}$ and the silica phase $I_{\mathrm{S}^*}$ are defined analogously. An exemplary 2D cutout of the phase-wise segmentation is presented in Figure 1b, where the pore phase is indicated gray, the AT phase white and the silica phase black. An object-wise segmentation of this image is shown in Figure 1c, see also Sections 2.4.2 and 2.4.3 below.

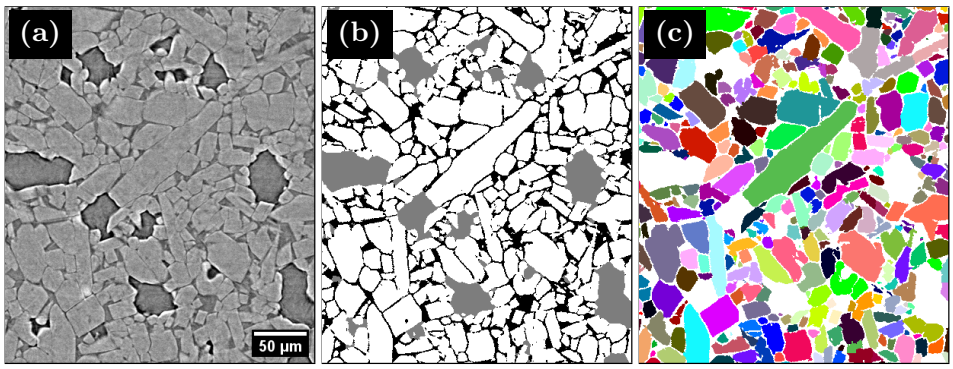


FIGURE 1. 2D cutout of the reconstructed SXCT tomogram (a), together with its phase-wise (b) and object-wise (c) segmentation. Note that false colors are utilized to identify different grains.

2.4.2. **Pore-wise segmentation.** To analyze the properties of individual pores, a pore-wise segmentation $I_{\mathrm{P}}$ of the pore phase image $I_{\mathrm{P}^*}$, defined in Section 2.4.1, is determined. Mathematically speaking, a mapping $I_{\mathrm{P}} \colon W \mapsto \{0, \dots, m_{I_{\mathrm{P}}}\}$ is computed, which is given by

$$I_{\mathrm{P}}(x) = \begin{cases} i, & \text{if } I_{\mathrm{P}^*}(x) = 1 \text{ and } x \text{ corresponds to the } i\text{-th pore,} \\ 0, & \text{else,} \end{cases}$$

for each $x \in W$, where $m_{I_{\mathrm{P}}} \in \mathbb{N} = \{1, 2, \dots\}$ denotes the number of individual pores.

For this, the Euclidean distance transformation $D_{\mathrm{P}} \colon W \mapsto [0, \infty)$ from the pore phase to its complement is determined [35]. More precisely, each voxel is assigned with its distance to the closest voxel belonging to either the AT or the silica phase. Note that $-D_{\mathrm{P}}$ can be considered as a topographical map, where the value of $D_{\mathrm{P}}(x)$ represents the depth at position $x \in W$. Typically, local minima of $-D_{\mathrm{P}}$ are utilized as markers for a marker-based watershed transform [36–38], where each local minimum serves as a marker for a single pore. Roughly speaking, in the watershed transform the basins of the topographical map $-D_{\mathrm{P}}$ are filled with water, by an uniformly rising water level, where each of these basins represents an individual pore.

However, a direct application of this procedure to the image data considered in the present paper would lead to severe oversegmentation, that is, the pore phase would be decomposed into too many and too small pores. A possible strategy to avoid oversegmentation is the so-called morphological reconstruction [20, 39], which thins out the markers of the watershed transform. More precisely, let $-d_1, -d_2$ be two neighboring local minima of $-D_{\mathrm{P}}$ with $d_1 \geq d_2 \geq 0$. Furthermore, let $w \subset W$ be the watershed ridge, which is the surface where the two basins corresponding to $d_1$ and $d_2$ meet. Let $\bar{w} \in w$ denote the minimizer of the negative distance transform $-D_{\mathrm{P}}$ on the watershed ridge $w$ and $-\bar{d}$ the minimum of $-D_{\mathrm{P}}$ on $w$, that is, $-\bar{d} = -D_{\mathrm{P}}(\bar{w}) = \min_{x \in w} -D_{\mathrm{P}}(x)$. The two pores (i.e., basins) corresponding to $d_1$ and $d_2$ are merged if

$$\frac{\bar{d}}{d_2} > c \tag{1}$$

for some threshold $c \in [0,1]$. In the literature, see e.g., [39], it is also common to define $c = 1-\alpha$ and reformulate Eq. (1) as $\min_{x\in w} D_{\mathrm{P}}(x)/d_2 \geq 1-\alpha$ for some $\alpha \in [0,1]$.

The procedure described above is visualized in Figure 2a. Note that a value of $c = 1$ corresponds to the classical watershed transformation, without merging any pores, while $c = 0$ corresponds to merging all pores, resulting in one (not necessarily connected) pore. Since the actual choice of $c$ controls the degree of oversegmentation, we will refer to it as the refinement parameter $c$ in the following. Note that a good choice of $c$ is crucial for the goodness of the segmentation, as a too large value of $c$ still leads to oversegmentation. However, too small $c$ results in too few and too large pores, i.e. undersegmentation. For further information on morphological reconstruction, we refer to [39].

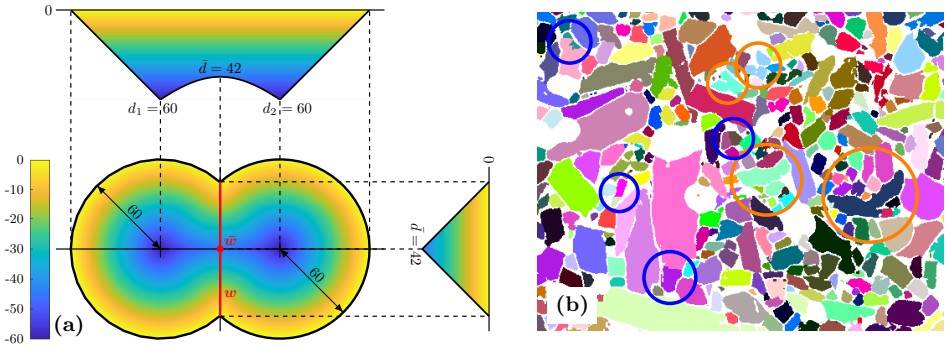


FIGURE 2. Scheme of the morphological reconstruction in 2D (a). The watershed ridge $w$ is highlighted in red with $\bar{d} = \min_{x\in w} -D_{\mathrm{P}}(x) = 42$. The classical watershed transform would lead to two regions, separated by the watershed ride $w$. In contrast, the morphological reconstruction merges these regions if $c < 42/60 = 0.7$. 2D cutout of a grain-wise segmentation (b), utilizing morphological reconstruction with refinement parameter $c = 0.75$, which leads to oversegmentation (blue circles) and undersegmentation (orange circles) simultaneously.

It turned out that a choice of $c = 0.1$ results in a reasonable pore-wise segmentation. After removing pores that exhibit a thickness of one voxel, as well as pores with a volume smaller than 100 voxels ($\widehat{=}37\,\mu\mathrm{m}^3$) the final segmentation $I_{\mathrm{P}}$ consists of $m_{I_{\mathrm{P}}} = 477$ pores. In the following, we will refer to a pore $P \subset W$ as the set of all voxels $x \in W$ for which $I_{\mathrm{P}}(x) = i$ for some $i \in \{1,\dots,m_{I_{\mathrm{P}}}\}$, and to $\mathcal{P}$ as the family containing all pores $P$.

2.4.3. **Grain-wise segmentation.** The grain-wise segmentation $I_{\mathrm{G}}\colon W \mapsto \{0,\dots,m_{I_{\mathrm{G}}}\}$ of the AT phase $I_{\mathrm{G}^*}$ introduced in Section 2.4.1 is defined as

$$I_{\mathrm{G}}(x) = \begin{cases} i, & \text{if } I_{\mathrm{G}^*}(x) = 1 \text{ and } x \text{ corresponds to the } i\text{-th grain,} \\ 0, & \text{else,} \end{cases}$$

for each $x \in W$, where $m_{I_{\mathrm{G}}} \in \mathbb{N}$ denotes the number of individual grains.

For this, each connected component of the AT phase with a volume smaller than 100 voxels ($\widehat{=}37\,\mu\mathrm{m}^3$) was removed. Furthermore, each connected component of the pore or silica phase, which is completely surrounded by the AT phase, is assigned to the AT phase.

Like in Section 2.4.2, a classical watershed transform would lead to oversegmentation. Moreover, since the grains are very inhomogeneous in size and degree of elongation, morphological

reconstruction would lead, depending on the choice of the refinement parameter $c$, either to oversegmentation, undersegmentation, or even both phenomena simultaneously, see Figure 2b.

Recall Eq. (1), which means that the degree of over- and undersegmentation of the morphological reconstruction can be controlled by the refinement parameter $c$. A small value of $c$ corresponds to undersegmentation, e.g., the segmentation exhibits too large grains, whereas a large value of $c$ results in oversegmentation, e.g., too small grains. Note that in this application, undersegmented grains tend to be non-convex, whereas oversegmented grains show more convex shapes (see Figure 2b, orange and blue circles, respectively). Furthermore, it is generally known that the true grain shape is typically convex (which can also be easily verified in Figure 1), as the equilibrium shape of a crystal results from minimizing its anisotropic surface free energy under the constraint of constant volume [40]. This motivates the iterative application of morphological reconstruction with increasing refinement parameters $c_0 < \ldots < c_n$ to generate a family of $n$ grain-wise segmentations $I_{\mathrm{G}}^{(c_0)}, \ldots, I_{\mathrm{G}}^{(c_n)}$ for some integer $n \in \mathbb{N}$, which exhibit an increasing number of grains with shrinking volumes and increasing convexity. Note that a grain $G \subset W$ is classified as correctly segmented if it is sufficiently convex. To quantify the convexity of a grain $G \subset W$, we consider the ratio

$$c(G) = \frac{V(G)}{V(q(G))} \in [0,1],$$

where $V(\cdot)$ denotes volume and $q(G)$ the convex hull of $G$. For the two-dimensional case, the concept of convexity is illustrated in Figure 5a.

Analogously to the pore-wise segmentation, let $D_{\mathrm{G}} \colon W \mapsto [0,\infty)$ denote the Euclidean distance transformation, which associates each voxel $x \in W$ with its distance to the closest voxel belonging either to the pore or silica phase. The local minima of $-D_{\mathrm{G}}$ are utilized to determine the segmentation $I_{\mathrm{G}}^{(c_i)} \colon W \mapsto \{0, \ldots, m_{c_i}\}$ for each $i \in \{0, \ldots, n\}$, where $m_{c_i} \in \mathbb{N}$ is the number of grains corresponding to the segmentation $I_{\mathrm{G}}^{(c_i)}$. Note that each segmentation $I_{\mathrm{G}}^{(c_i)}$ is based on a watershed transform, followed by morphological reconstruction with refinement parameter $c_i \in [0,1]$. Furthermore, let $\mathcal{G}^{(c_i)} = \{G_1^{(c_i)}, \ldots, G_{m_{c_i}}^{(c_i)}\}$ represent the family of grains corresponding to $I_{\mathrm{G}}^{(c_i)}$, where $G_j^{(c_i)} = \{x \in W \colon I_{\mathrm{G}}^{(c_i)}(x) = j\}$ for each $j \in \{1, \ldots, m_{c_i}\}$.

Furthermore, the following algorithm is used to successively create correctly segmented grains. Let $\mathcal{G} = \emptyset$ be the initial family of correctly segmented grains. For increasing $i \in \{0, \ldots, n-1\}$, the grain $G_j^{(c_i)} \in \mathcal{G}^{(c_i)}$ for each $j \in \{1, \ldots, m_{c_i}\}$ is added to $\mathcal{G}$ if $c(G_j^{(c_i)}) > t_{\mathrm{conv}}$ for some threshold $t_{\mathrm{conv}} \in [0,1]$ and $G_j^{(c_i)} \cap G = \emptyset$ for all $G \in \mathcal{G}$. This ensures that all grains $G \in \mathcal{G}$ are sufficiently convex and pairwise disjoint.

This procedure is motivated by Eq. (1), which implies that for any refinement parameter $c_i < c_\ell$ (and thus $i < \ell$) each grain $G_j^{(c_i)}$ of the segmentation $I_{\mathrm{G}}^{(c_i)}$ can be represented as union of several grains $G_k^{(c_\ell)} \in \mathcal{G}^{(c_\ell)}$ of $I_{\mathrm{G}}^{(c_\ell)}$. Thus, for each $j \in \{1, \ldots, m_{c_i}\}$ we have

$$G_j^{(c_i)} = \bigcup_{k \in K} G_k^{(c_\ell)},$$

for some index set $K \subset \mathbb{N}$ with cardinality $\#K \geq 1$. Furthermore, if $G_j^{(c_i)}$ breaks down into several smaller grains $G_k^{(c_\ell)}$, that is, $\#K > 1$, each $G_k^{(c_\ell)}$ is smaller and typically more convex than $G_j^{(c_i)}$.

To avoid too small grains, which would arise from further increasing the refinement parameter, all grains $G^{(c_n)} \in \mathcal{G}^{(c_n)}$ corresponding to the last segmentation $I_{\mathrm{G}}^{(c_n)}$ are added to $\mathcal{G}$ if $G^{(c_i)} \cap G = \emptyset$ for all $G \in \mathcal{G}$. Note that this may add grains $G$ to $\mathcal{G}$, with convexity $c(G) \leq t_{\mathrm{conv}}$.

Through experimentation and visual inspection it turned out that

$$c_0 = 0.5, c_1 = 0.55, c_2 = 0.6, \ldots, c_8 = 0.9$$

and $t_{\text{conv}} = 0.55$ serve as a good choice of parameters to balance out over- and undersegmentation of the present data set. Figure 3 displays the evolution of the set of correctly segmented grains $\mathcal{G}$ for different steps of the iterative morphological reconstruction.

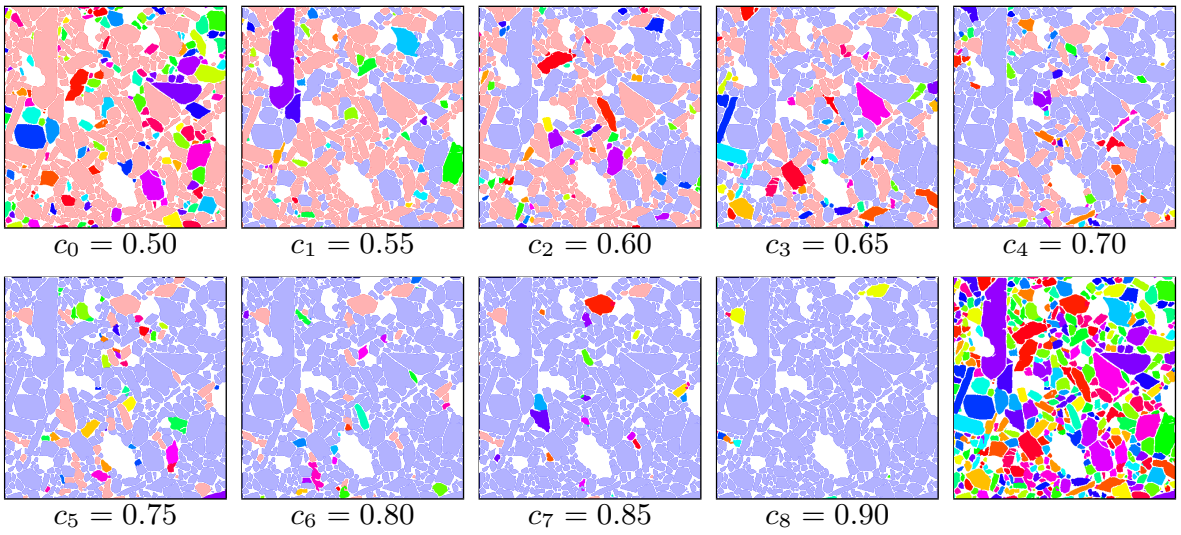


FIGURE 3. Intermediate steps of the morphological reconstruction. In each step, correctly segmented grains, which area added to $\mathcal{G}$ are highlighted in different colors, whereas falsely segmented grains are shaded red. Grains that were already classified as correct in a previous step are indicated in blue shading. Note that falsely segmented grains are by construction undersegmented, e.g., multiple regions disconnected by background are labeled as a single grain.

Finally, after removing grains with a volume smaller than 10 voxels ($\widehat{=}3.7\,\mu\text{m}^3$), as well as grains with a thickness of only one voxel, the family of correctly segmented grains is denoted by $\mathcal{G} = \{G_1, \ldots, G_{m_{I_G}}\}$, with $m_{I_G} = 14\,114$. The grain-wise segmentation $I_G \colon W \mapsto \{0, \ldots, m_{I_G}\}$ is given by

$$I_G(x) = \begin{cases} i, & \text{if } x \text{ corresponds to grain } G_i, \\ 0, & \text{else,} \end{cases}$$

for each $x \in W$, see Figure 1c. Furthermore, to get a visual impression of the segmented grains, 3D renderings of exemplary grains for different size classes are shown in Figure 4. Note that although the iterative segmentation approach stated above drastically reduces over- and undersegmentation, there still remain some segmentation errors, see e.g. the bottom row in Figure 4 for size classes of 70 µm, 30 µm and 15 µm, where two different grains are classified as one grain.

2.5. **Geometric descriptors.** The segmentations $I_P$ and $I_G$, derived in Sections 2.4.2 and 2.4.3, allow the computation of various descriptors characterizing the size, shape, and spatial orientation of individual pores and grains. These descriptors reduce the complex voxelized 3D morphology to a single scalar number. In particular, this allows one to determine empirical probability distributions of these descriptors, which will be discussed in Section 3 below.

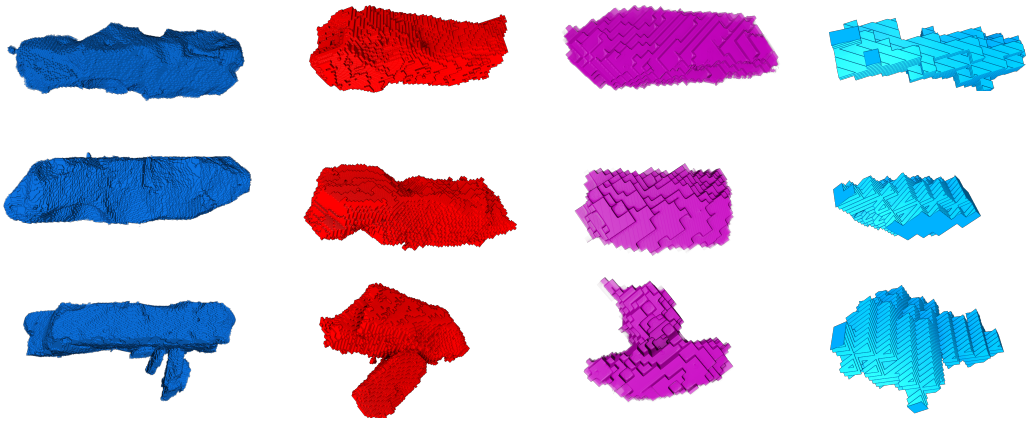


FIGURE 4. 3D renderings of exemplary segmented grains $G \in \mathcal{G}$ with different volume-equivalent diameter $d_3(G)$, which is formally introduced in Section 2.5.1 below. Note that the grains of all four size classes are scaled to appear visually comparable. Although the iterative application of morphological reconstruction drastically reduced the amount of over- and undersegmented grains, there still remain some undersegmented (non-convex) grains, see the bottom row for the size classes of 70 µm, 30 µm and 15 µm.

First, in Section 2.5.1 geometric descriptors characterizing the 3D morphology of individual pores and grains are introduced. Subsequently, in Section 2.5.2 more sophisticated geometric descriptors are considered that characterize the interaction between pores and grains. Finally, in Section 2.5.3, descriptors are defined to compare virtual 2D cross sections of grains, derived from 3D SXCT images with those of the 2D EBSD measurements. This builds on a previous paper [12], where the material, which is subject of the present study, was already analyzed using 2D descriptors, derived from 2D EBSD measurements. These 2D descriptors from different imaging techniques are compared with each other in Section 3.5.

2.5.1. **Geometric 3D descriptors of individual pores and grains.** In this section geometric descriptors are defined, which characterize the 3D morphology of pores and AT grains, derived trough the segmentation procedure considered in Sections 3.1 and 3.2, respectively.

Note that the following descriptors are defined for some set of voxels $G \subset W$, which represents either a pore or an AT grain. For simplification, $G$ will be called in the upcoming sections "grain", even though it can also represent pores.

**Volume-equivalent diameter.** The size of a grain $G \subset W$ is captured by its volume-equivalent diameter $d_3(G)$, being the diameter of a ball with the same volume as $G$, that is,

$$d_3(G) = \sqrt[3]{\frac{6v_3(G)}{\pi}},$$

where $v_3(G)$ is the volume of $G$, which is approximated by the number of voxels assigned to $G$.

**Convexity.** The convexity $c_3(G) \in [0,1]$ of a grain $G \subset W$ is defined as the quotient

$$c_3(G) = \frac{v_3(G)}{v_3(q(G))}$$

of the volume $v_3(G)$ of $G$ divided by the volume $v_3(q(G))$ of its convex hull $q(G)$.

**Aspect ratio.** The aspect ratio $e_3(G)$ of a grain $G = \{x_1, \dots, x_n\} \subset W$, consisting of $n$ voxels for some $n \in \mathbb{N}$, is determined analogously to the procedure considered in [41], that is, by computing the ratio of the lengths of the minor and major axes of a best-fitting ellipsoid, which is derived by a principal component analysis (PCA) [42]. More precisely, consider the voxels $x_1, \dots, x_n \in W$ as point cloud in the 3-dimensional Euclidean space $\mathbb{R}^3$. By applying a PCA to this point cloud, the orthonormal principal directions $a_1, a_2, a_3 \in \mathbb{R}^3$ of the fitted ellipsoid are derived. Note that $a_1$ points in the direction of the major axis, $a_2$ in the direction of the intermediate axis, and $a_3$ in the direction of the minor axis of the fitted ellipsoid. The lengths corresponding to the axes of the fitted ellipsoid are denoted by $\ell_1, \ell_2$ and $\ell_3$, where it holds that $\ell_3 \leq \ell_2 \leq \ell_1$. Finally, the aspect ratio $e_3(G)$ of $G$ is given by

$$e_3(G) = \frac{\ell_3}{\ell_1} \in [0, 1].$$

Note that $e_3(G) = 1$ implies that $\ell_1 = \ell_2 = \ell_3$, corresponding to a spherical best-fitting ellipsoid and, consequently, a spherical grain $G$. A decreasing value of $e_3(G)$ indicates more an elongated ellipsoid, but does not specify whether the shape is oblate (e.g. "discuss-shaped") or prolate (e.g. "cigar-shaped"). A 2D visualization of two grains with similar volume-equivalent diameters, but different convexities and aspect ratios is shown in Figure 5a.

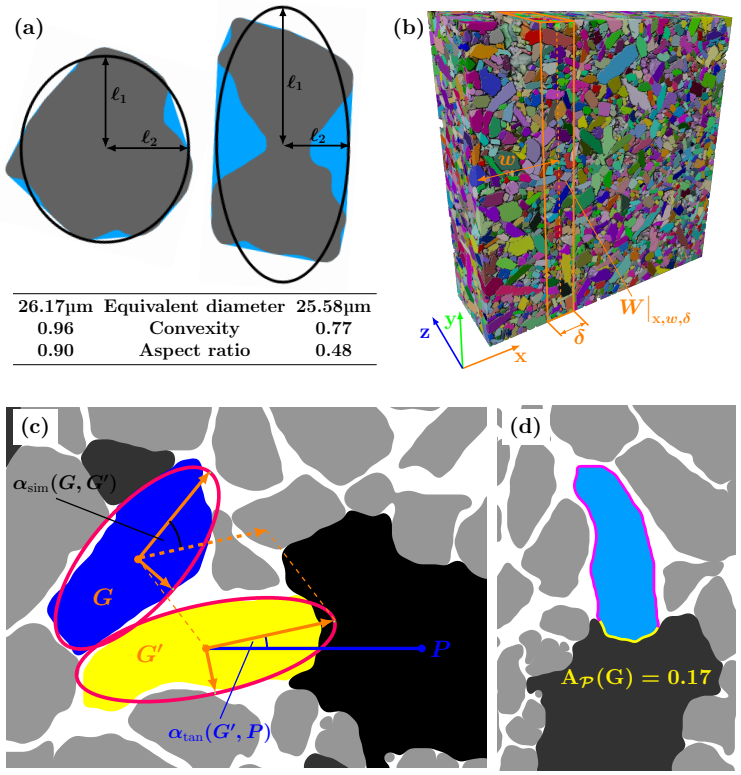


FIGURE 5. (a) Schematic 2D representations of two grains (gray) and their convex hulls (blue), having similar volumes but different convexities and aspect ratios. (b) Illustration of the sliding window approach and (c) orientation similarity and tangentiality. (d) The proportional shared surface of a grain with a pore, defined as the fraction of the grain's surface area (magenta) that is shared with a pore (yellow).

**Orientation similarity.** The orientation similarity $\alpha_{\mathrm{sim}}(G, G') \in [0,1]$ refers to the similarity between the directions $a_1, a_1' \in \mathbb{R}^3$ of the major axes of two grains $G, G' \subset W$. It is given by $\alpha_{\mathrm{sim}}(G, G') = |\langle a_1, a_1' \rangle|$, where $\langle a_1, a_1' \rangle$ denotes the dot product of $a_1$ and $a_1'$. Note that $\alpha_{\mathrm{sim}}(G, G') = 1$ corresponds to a parallel alignment, while $\alpha_{\mathrm{sim}}(G, G') = 0$ indicates that $a_1$ and $a_1'$ are perpendicular. An illustration of this descriptor is given in Figure 5c.

**Sliding window approach.** The geometric descriptors stated above are utilized in Section 3 to determine (bivariate) kernel density estimates. Additionally, the volume-equivalent diameter and aspect ratio are used to analyze the directional behavior of grains, employing a sliding window approach. For that, let

$$W\big|_{\mathrm{x},w,\delta} = W \cap \{w - \delta/2, w + 1 - \delta/2, \ldots, w + \delta/2\} \times \mathbb{N} \times \mathbb{N} \tag{2}$$

denote the restricted window of thickness $\delta + 1 \in \mathbb{N}$ for an even integer $\delta \geq 0$ centered on $w \in \mathbb{N}$ along the x-axis. The concept of a restricted window is depicted in Figure 5b.

Furthermore, let $d_3(W\big|_{\mathrm{x},w,\delta})$ denote the collection of volume-equivalent diameters $d_3(G)$ of grains $G \subset W$, whose centroid $\xi(G) \in \mathbb{R}^3$ is located in the convex hull $q(W\big|_{\mathrm{x},w,\delta})$ of $W\big|_{\mathrm{x},w,\delta}$. Note that the centroid $\xi(G)$ of a grain $G$ is defined by component-wise averaging as $\xi(G) = (\bar{x}, \bar{y}, \bar{z})$, where $\bar{x}$ is given by

$$\bar{x} = \frac{1}{\#G} \sum_{(x,y,z) \in G} x,$$

and $\bar{y}$ and $\bar{z}$ are determined analogously.

Similarly, $e_3(W\big|_{\mathrm{x},w,\delta})$ and $c_3(W\big|_{\mathrm{x},w,\delta})$ denote the collections of aspect ratios $e_3(G)$ and convexities $c_3(G)$ of grains $G \subset W$, whose centroid $\xi(G)$ is located in $W\big|_{\mathrm{x},w,\delta}$. In addition, the number of grains $G$, whose centroid $\xi(G)$ is located within the convex hull of the restricted window $W\big|_{\mathrm{x},w,\delta}$ is denoted by $N(W\big|_{\mathrm{x},w,\delta})$. Finally, we consider the volume fraction $\varepsilon_{I_{\mathrm{G}^*}}(W\big|_{\mathrm{x},w,\delta})$ of the AT phase in the restricted window $W\big|_{\mathrm{x},w,\delta}$, which is defined as

$$\varepsilon_{I_{\mathrm{G}^*}}(W\big|_{\mathrm{x},w,\delta}) = \frac{\#\{x \in W\big|_{\mathrm{x},w,\delta} \text{ with } I_{\mathrm{G}^*}(x) = 1\}}{\#W\big|_{\mathrm{x},w,\delta}},$$

where $I_{\mathrm{G}^*} \to \{0,1\}$ denotes the binary image corresponding to the AT phase, see Section 2.4.1. The quantities introduced above are defined analogously with respect to the y- and z-axes.

2.5.2. **Relational descriptors of pore–grain phase.** We now introduce more sophisticated geometric descriptors that characterize the interaction between pores and grains.

**Number of neighboring grains.** For any $r \geq 0$, let $\mathrm{dil}_r(G) \subset \mathbb{R}^3$ denote the dilation [33] of a grain $G$ with a ball-shaped structuring element with radius $r$. Then, putting $r = 1$, the number of neighboring grains $N_{\mathrm{neigh}}(G)$ of $G$ is given by the number of grains which intersect with the set $\mathrm{dil}_1(P)$, that is,

$$N_{\mathrm{neigh}}(G) = \#\{G \in \mathcal{G} \colon G \cap \mathrm{dil}_1(G) \neq 0\},$$

where $\mathcal{G}$ denotes the family of all (correctly segmented) grains $G \subset W$.

**Proportional shared surface.** The proportional surface $A_{\mathcal{P}}(G) \in [0,1]$ that a grain $G \in \mathcal{G}$ shares with the family $\mathcal{P}$ of all pores $P \subset W$ is given by

$$A_{\mathcal{P}}(G) = \frac{\mathcal{H}_2\big(\partial G \cap (\cup_{P \in \mathcal{P}} \partial P)\big)}{\mathcal{H}_2(\partial G)},$$

where $\mathcal{H}_2(\cdot)$ denotes the 2-dimensional Hausdorff measure in $\mathbb{R}^3$, which is used here to quantify the surface area of interfaces. The quantity $A_{\mathcal{P}}(G)$ is computed on voxelized image data using the algorithm proposed in [43]. A value of $A_{\mathcal{P}}(G) = 1$ indicates that $G$ is completely surrounded by the pore phase, whereas $A_{\mathcal{P}}(G) = 0$ corresponds to no joint surface between $G$ and the pore phase. A 2D visualization of the proportional shared surface of a grain is shown in Figure 5d.

**Distance to pore phase.** The (minimum) distance $\operatorname{dist}_{\mathcal{P}}(G) > 0$ of a grain $G \in \mathcal{G}$ to the pore phase $\bigcup_{P\in\mathcal{P}} P$ is given by

$$\operatorname{dist}_{\mathcal{P}}(G) = \min_{x\in G, y\in\bigcup_{P\in\mathcal{P}} P} \|x - y\|,$$

where $\|\cdot\|$ denotes the Euclidean norm in $\mathbb{R}^3$.

**Tangentiality.** Of particular interest is whether the grains arrange in certain patterns around the pores, that is, whether the grains align tangentially to the surface of the pores. This is equivalent to whether the major axes of the best-fitting ellipsoids of the grains are perpendicular to the normal vector of the pore surface. Since determining normals (or tangent planes) of voxelized objects is challenging, a practical substitute for the normal vector is the connection vector between the centroids $\xi(P), \xi(G) \in \mathbb{R}^3$ of a pore $P \in \mathcal{P}$ and its neighboring grain $G \in \mathcal{G}$. Then, the normalized vector $v_{G,P} \in \mathbb{R}^3$, which points from $\xi(G)$ towards $\xi(P)$ is given by

$$v_{G,P} = \frac{\xi(G) - \xi(P)}{\|\xi(G) - \xi(P)\|},$$

and the tangentiality $\alpha_{\tan}(G, P) \in [0, 1]$ of $G$ with respect to $P$ is defined as

$$\alpha_{\tan}(G, P) = |\langle v_{G,P}, a_1\rangle|,$$

where $a_1$ is the direction of the major axis of the best-fitting ellipsoid of $G$. Note that the tangentiality $\alpha_{\tan}(G, P)$ of $G$ with respect to $P$ measures the arrangement between the connection vector $v_{G,P}$ and the direction of the major axis $a_1$ of $G$. A tangentiality of $\alpha_{\tan}(G, P) = 0$ indicates a perpendicular arrangement of the connection vector $v_{G,P}$ and the direction of the major axis $a_1$, suggesting a tangential arrangement of $G$ with respect to the surface of the pore. On the other hand, a tangentiality of $\alpha_{\tan}(G, P) = 1$ indicates parallel alignment. A 2D sketch of the notion of tangentiality is shown in Figure 5c.

2.5.3. **Geometric 2D descriptors.** The focus of this paper is on the statistical description of the 3D properties of pores and grains, observed in aluminum ceramics. However, in [12], the area-equivalent diameter (grain size) as well as the aspect ratio (shape factor) of the same sample were analyzed utilizing 2D EBSD images. In the following, we determine these quantities for 2D cross sections, taken from segmented 3D SXCT image data, and compare them in Section 3.5 with the results of [12].

In accordance with the previously introduced geometric 3D descriptors, we define analogous descriptors for 2D cross sections, where the cross sections of pores and grains will be considered as two-dimensional objects. To keep the notation as simple as possible, we will use the same kind of symbols as we used until now. In particular, the sampling window still bears the notation $W \subset \mathbb{N} \times \mathbb{N}$, and the grains are denoted by $G \subset W$.

**Area-equivalent diameter.** The area-equivalent diameter $d_2(G)$ of a grain cross section $G \subset W$ is given by

$$d_2(G) = \sqrt{\frac{4v_2(G)}{\pi}},$$

where $v_2(G)$ denotes the area of $G$, which is approximated by the number of pixels assigned to the grain cross section $G$.

**Aspect ratio.** Similarly to the definition of the three-dimensional aspect ratio introduced in Section 2.5.1, a grain cross section $G = \{x_1, \dots, x_n\}$, consisting of $n$ pixels for some $n \in \mathbb{N}$, is considered a point cloud of $n$ points $x_1, \dots, x_n$ in the two-dimensional Euclidean space $\mathbb{R}^2$. By applying a principal component analysis, the directions $a_1, a_2 \in \mathbb{R}^2$ of the major and minor axes of a best-fitting ellipse are derived. The lengths of the major and minor axes are denoted by $\ell_1$ and $\ell_2$, respectively. The aspect ratio $e_2(G)$ of a grain cross section $G$ is then given by $e_2(G) = \ell_2/\ell_1$, representing the ratio of the lengths of the minor and major axes.

## 3. Results and discussion

In this section, the probability densities of the geometric descriptors introduced in Section 2.5 are determined for both the pores and the AT grains. Note that the morphology of individual pores and grains is based on the segmentation methods pointed out in Sections 2.4.2 and 2.4.3. To avoid edge effects, only pores and grains that are fully contained within the sampling window $W$ are considered. Probability densities were computed using kernel density estimation, as implemented in [44], with bandwidth selection based on Scott's rule [45].

### 3.1. Statistical analysis of pores.

Recall that in Section 2.5 several geometric descriptors were introduced to describe the size and shape of the pores. Figure 6a shows the probability density of the volume-equivalent diameter $d_3(P)$ of the pores $P \subset W$, which exhibits a bimodal shape with peaks at approximately 5 µm and 29 µm.

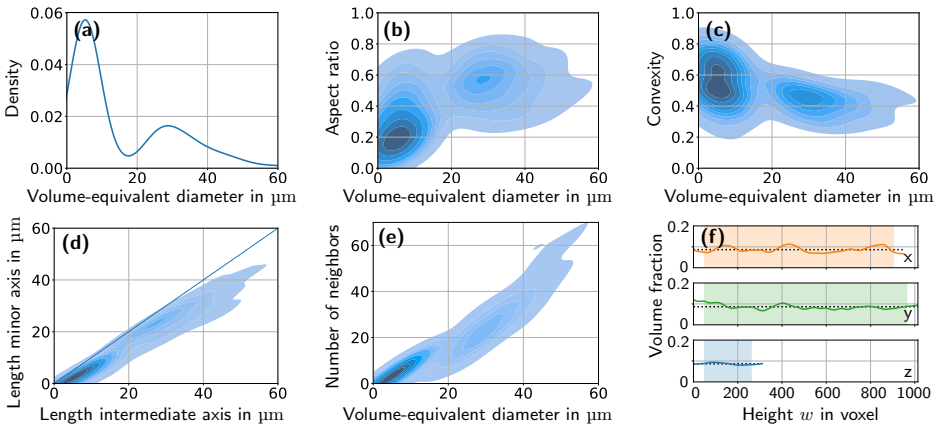


Figure 6. Univariate probability density of the volume-equivalent pore diameter $d_3(P)$ (a), bivariate probability densities of pairs of geometric pore descriptors (b)-(e), the volume fraction $\varepsilon_{I_{P^*}}(W|_{\cdot,w,\delta})$ of the restricted window $W|_{\cdot,w,\delta}$ centered at height $w \in \{51, 52, \dots, \}$ with thickness $\delta + 1 = 101$, where the dotted lines indicate the global volume fractions (f).

The bivariate probability densities of the volume-equivalent diameter $d_3(P)$ and the aspect ratio $e_3(P)$, as well as the volume-equivalent diameter $d_3(P)$ and convexity $c_3(P)$ are shown in Figures 6b and 6c, respectively. These densities suggest that larger pores tend to be less elongated and less convex, where the correlation between volume-equivalent diameter and convexity is a bit less pronounced, compared to the correlation between volume-equivalent diameter and aspect ratio. In essence, Figures 6b and 6c confirm the visual impression of Figure 6a, that the

pore phase consists of two populations of pores. One population contains small pores, which are strongly elongated and relatively convex, and the other population consists of larger pores, which are less convex and less elongated.

Figure 6d shows the bivariate probability density of the lengths of the intermediate axis $\ell_2(P)$ and the minor axis $\ell_3(P)$ of pores. The diagonal line represents the angle bisectrix, which indicates pairs of equal values; e.g., points on this line correspond to pores where the lengths of intermediate and minor axes are the same. Therefore, Figure 6d suggests that, independently of the lengths of these axes, the intermediate and minor axes are approximately equal in length, which implies a prolate shape of the pores. Finally, Figure 6e shows the bivariate probability density of the number of neighbors and the volume-equivalent diameter. It indicates that, as expected, larger pores tend to have more neighboring grains than smaller ones.

These findings can be rationalized through the sintering process. During powder mixing and compaction, imperfect particle packing leaves inter-agglomerate voids that emerge after sintering as relatively large blunt pores [46]. When the compact is fired at 1500–1600°C, densification first drives a general reduction of the free surface energy by shrinking porosity, then the grain boundary energy falls as the grains grow, and finally the grains elongate along their crystallographic a-axis to further reduce the boundary area. This anisotropic growth confines residual voids, stretching them into highly prolate ("cigar-shaped") intergranular pores, while the original compaction voids change only slightly because sluggish $Al_2TiO_5$ sintering kinetics limit their interaction with surrounding grains [47, 48]. The resulting bimodal pore size distribution (i.e., the coarse, low-convexity pores inherited from compaction and the fine, elongated pores formed during sintering) is indicative of the combined thermodynamic forces of surface energy minimization and anisotropic grain growth, highlighting the fact that the sintering process employed still falls short of full densification.

The results of the sliding window analysis of the volume fraction of the pore phase, using a restricted window $W\big|_{\cdot,\cdot,\delta}$ with a thickness of $\delta + 1 = 101$ voxels, are presented in Figure6f. Shaded areas indicate the interval where the restricted window $W\big|_{\cdot,\cdot,\delta}$ is completely contained in the sampling window $W$. Outside this range, intersections with the sampling window $W$ may introduce edge effects. The volume fractions $\varepsilon_{I_{\mathrm{P}^*}}(W\big|_{\cdot,w,\delta})$ exhibit a relatively homogeneous distribution throughout the entire sampling window $W$, along all three directions. The other descriptors investigated with the sliding window approach, namely volume-equivalent diameter $d_3(W\big|_{\mathrm{x},w,\delta})$, aspect ratio $e_3(W\big|_{\mathrm{x},w,\delta})$, convexity $c(W\big|_{\mathrm{x},w,\delta})$ and number of pores $N(W\big|_{\mathrm{x},w,\delta})$, show similar homogeneous behaviors. These results indicate an even spatial distribution of porosity within the sampling window $W$, regardless of the investigated direction.

3.2. **Statistical analysis of grains.** In this section, the descriptors introduced in Section 2.5 are analyzed for individual grains. Motivated by the bimodal pore size distribution, revealed in Section 3.1, each grain $G$ is classified as neighboring a small pore (SP), neighboring a large pore (LP), or not neighboring any pore (NP), where a pore $P \subset W$ is considered as "small", if $d_3(P) < 17.5\,\mu\mathrm{m}$, and as "large" if $d_3(P) \geq 17.5\,\mu\mathrm{m}$. The threshold of 17.5 µm corresponds approximately to the local minimum observed in the probability density of the volume-equivalent diameters of the pores, see Figure 6a. This subdivision splits the set of AT grains $\mathcal{G}$ into three subsets with 295 grains neighboring small pores, 5893 grains neighboring large pores, and 7499 grains neighboring no pores. Additionally, 1027 grains, which neighbor multiple pores, are excluded from this classification.

Figure 7a suggests that the grain size distribution is bimodal, showing peaks at $\approx 5\,\mu\mathrm{m}$ and $\approx 17\,\mu\mathrm{m}$. However, the bimodal shape differs for the three grain classes. Within the NP class,

the two peaks are approximately of the same size, whereas for SP and LP the peak corresponding to larger grains is significantly more pronounced. Additionally, SP grains tend to be larger than the other ones. The aspect ratios in all three grain classes show a similar behavior, as shown in Figure 7b. Figure 7c presents the bivariate probability densities of volume-equivalent diameter and aspect ratio for all grains. The corresponding bivariate densities for each of the grain classes NP, SP, and LP reveal a similar correlation structure, that is, larger grains tend to have a smaller aspect ratio, indicating a more elongated shape. Furthermore, note that the intermediate and minor axes of grains have approximately equal lengths for the entire family of all grains, see Figure 7d. Analogous investigations for the grain classes NP, SP and LP imply similar bivariate probability densities. Taken together, the overall grain shape is prolate, where larger grains tend to be more elongated, which is also confirmed by the 3D grain renderings for different grain size classes shown in Figure 4.

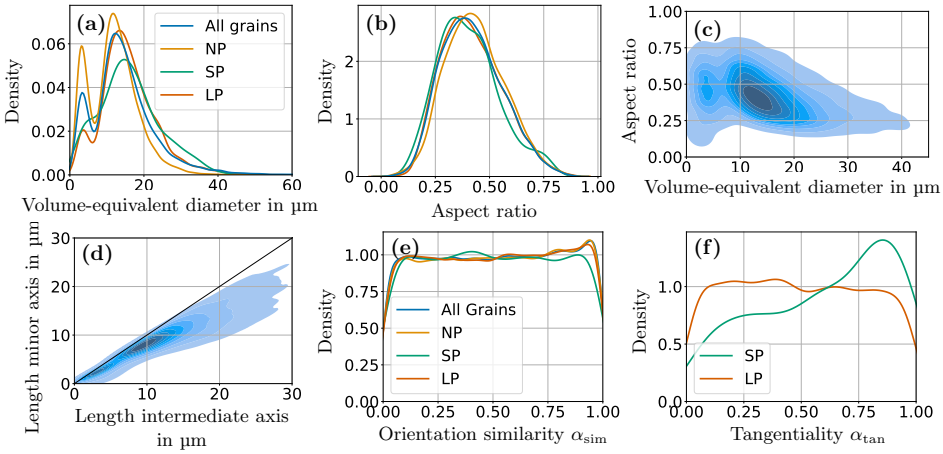


FIGURE 7. Univariate probability density of the volume-equivalent grain diameter (a) and aspect ration (b), together with their (joint) bivariate density (c), and the bivariate density of the lengths of the intermediate and minor axes (d), for the entire family of all grains. The univariate probability density of orientation similarity for all pairs of grains and for pairs of NP-, SP- and LP-grains (e), as well as tangentiality of SP-and LP-grains (f).

The occurrence of a bimodal grain population (i.e. large and small grains) can be linked to the bimodal pore size distribution and reflects the complex interplay of thermodynamic and microstructural factors during sintering. Large pores appear to hinder grain growth by constraining mass transport and limiting boundary mobility, while small pores may actually enhance local grain coarsening due to their high surface energy, which drives atomic diffusion and promotes Ostwald ripening [49–51]. This effect leads to an accelerated growth of grains adjacent to small pores, which explains the scarcity of fine grains in such regions. Abnormal grain growth (AGG) further contributes to this bimodal distribution, as energetically favorable large grains consume smaller ones during sintering. The resulting prolate morphology of the grains and pores is induced by the crystallographic anisotropy of $Al_2TiO_5$, where grains elongate along the a-axis ([100] direction), minimizing the energetically costly grain boundary surfaces perpendicular to this direction [47, 52]. Thus, the final microstructure (i.e., elongated grains and pores) is the result of a combination of anisotropic grain growth, pore-induced local diffusion enhancement, and energy-driven coarsening mechanisms.

To assess whether grains have locally preferred spatial orientations, the orientation similarity $\alpha_{\text{sim}}(G, G')$ was analyzed only for grains $G, G' \subset W$ that are close together. More precisely, grains $G$ and $G'$ are considered to be close to each other if the minimal distance between them does not exceed the value of 3.6 µm ($\widehat{=}$5 voxels), that is, $\min_{x \in G, x' \in G'} |x - x'| \leq 3.6\,\mu\text{m}$. Recall that a value of $\alpha_{\text{sim}}(G, G') = 0$ corresponds to a perpendicular arrangement between $G$ and $G'$, while $\alpha_{\text{sim}}(G, G') = 1$ implies their parallel alignment. As shown in Figure 5e, the probability density remains approximately constant for all $\alpha_{\text{sim}} \in [0, 1]$, suggesting that the grains do not exhibit a locally preferred orientation, regardless of their classification.

In addition, tangentiality $\alpha_{\text{tan}}(G)$ describes the orientation of a grain $G \subset W$ relative to its neighboring pore $P \subset W$. Recall that a value of $\alpha_{\text{tan}}(G) = 0$ suggests that $G$ is tangentially arranged to the surface of the pore, whereas $\alpha_{\text{tan}}(G) = 1$ implies a normal arrangement. As shown in Figure 7f, grains adjacent to large pores exhibit a uniform directional arrangement. In contrast, grains that neighbor small pores tend to align more normally with respect to the surface of the pore. Moreover, the bivariate densities shown in Figures 8a and 8d, suggest that there is no significant correlation between the volume-equivalent diameter of the grains and their tangentiality.

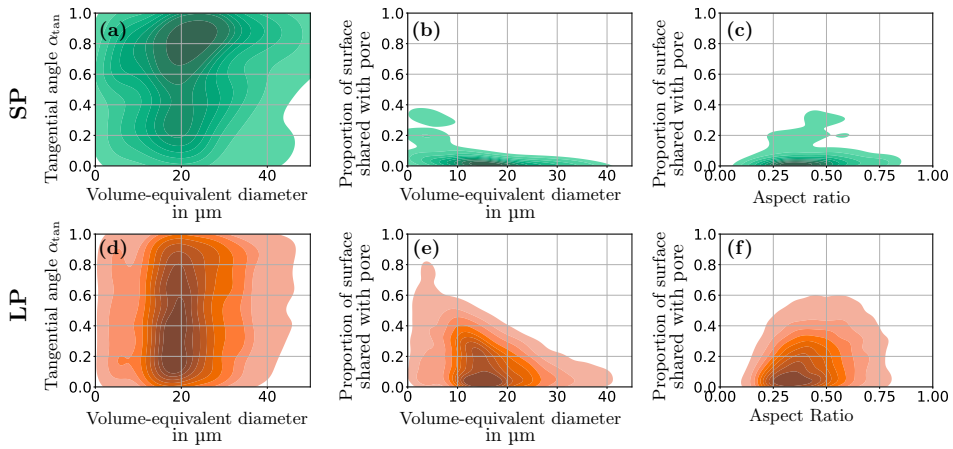


FIGURE 8. Bivariate probability densities of various pairs of geometric grain descriptors, for SP-grains (a)-(c), and for LP-grains (d)-(f).

For the analysis of local heterogeneities, AT grains within a moving restricted window $W\big|_{\cdot,\cdot,\delta}$ with $\delta + 1 = 51$ voxels were considered to investigate their volume fraction, number, volume-equivalent diameter, and aspect ratio. Since these four descriptors exhibit constant values throughout the entire sampling window $W$ in the three spatial directions, the presentation of the corresponding graphs is omitted for the sake of brevity. Anyhow, these results indicate a homogeneous distribution of the AT phase within the sampling window $W$.

The bivariate densities of the proportion of the surface of grains, shared with pores, and the volume-equivalent diameter of grains are shown in Figures 8b and 8e for the SP- and LP-grains, respectively. Similarly, the bivariate densities of the proportion of the surface of grains, shared with pores, and the aspect ratio of grains are shown in Figures 8c and 8f. All four bivariate probability densities indicate that there is no apparent relationship between these descriptors. These observations suggest that the growth direction of $Al_2TiO_5$ grains is primarily governed by their crystallographic orientation rather than by the influence of a free surface [50]. This conclusion aligns with previous, unpublished, findings. In these studies, unusual X-ray

diffraction (XRD) patterns were observed near the surfaces of sintered $Al_2TiO_5$ samples, with peak intensities significantly deviating from standard data, suggesting a possible surface-driven grain orientation effect. However, these anomalies disappeared when the surface layer was removed through machining, and the XRD results from the interior of the samples matched the expected reference patterns. In the current study, such surface effects were not detected via X-ray computed tomography, which is consistent with the fact that all sample surfaces had been machined prior to analysis, effectively eliminating any potential surface-influenced microstructural features.

3.3. **Qualitative analysis of silica.** Since a phase segmentation into pores, AT grains, and silica was performed in Section 2.4.1, a comprehensive analysis of the three phases would be natural. However, phase segmentation relies on hand labeling, which was primarily focused on achieving an accurate grain-wise segmentation. This was accomplished by enforcing the separation of adjacent grains through a thin layer of silica, leading to an overestimation of the silica phase by volume, see Figure 1. Furthermore, the silica phase consists of thin layers whose morphologies are highly sensitive to misclassified voxels making a reliable quantitative analysis challenging.

Despite the inherent bias in the morphology and volume fraction of the silica phase, a qualitative analysis remains feasible. To investigate the volume fraction of the silica phase, a sliding window approach with a restricted window $W\big|_{\cdot,w,\delta}$ with thickness $\delta + 1 = 1$ was performed. Similarly to the volume fractions of the pore phase (see Figure 6f) and the AT phase, the silica phase shows a homogeneous behavior, indicating a homogeneous spatial distribution throughout the entire sampling window $W$.

Consequently, by overestimating the volume fraction of the silica phase, the volume fraction of the AT phase is underestimated. However, since the AT phase has a clearly higher volume fraction, and the shape of individual grains is more bulky, the affectation of misclassified voxels is negligible and was not taken into account in the previous analysis of the AT phase.

3.4. **Phase and grain segmentation of the "flexible" material.** The segmentation approach stated in Section 2.4 was also applied to a second aluminum titanate ceramic, referred to as the "flexible" (F) scenario, introduced in Section 2.1. This material differs from the previously discussed "very flexible" (VF) material by a shorter dwell time during sintering. For a detailed comparison between AT-F and AT-VF, we refer to Table 1.

The results of the segmentation procedure for AT-F are presented in Figure 9. From the raw SXCT image (Figure 9a) it is evident, that obtaining a reliable and trustworthy segmentation, even by the human eye, is very challenging, if not impossible. Therefore, we have not conducted a detailed analysis for the flexible scenario as we did for the very flexible one.

However, a comparison of the probability densities of area-equivalent diameters and aspect ratios of virtual cross sections of grains obtained from segmented 3D SXCT images with those derived from EBSD images reveals a notable similarity, see Figures 10c and 10d. This implies that even for features of a scale similar to the resolution, the presented segmentation procedure can derive appropriate results. For a detailed discussion of the comparison between virtual SXCT cross sections and 2D EBSD images, see Section3.5.

3.5. **Comparison of virtual SXCT cross sections and EBSD data.** In this section, the results of the analysis of 2D EBSD images, which were presented in a previous paper [12], are compared to those obtained for virtual 2D cross sections derived from 3D SXCT reconstructions. More precisely, these virtual 2D cross sections can be considered as restricted windows $W\big|_{\cdot,w,\delta}$

as defined in Eq. (2) with $\delta + 1 = 1$ and some equidistant distance of $w = 36\,\mu\text{m}$ ($\widehat{=}\,50$ voxels). To ensure consistency and eliminate biases from the methods used in [12] and the present paper, all quantities were determined utilizing the methods described in Section 2.5.3. Furthermore, to avoid edge effects, the cross sections of grains cut off by the 2D sampling window $W\big|_{\cdot,w,1}$ or the sampling window of the 2D EBSD image were not considered. It is important to note that because the EBSD measurements do not distinguish between the pore phase and the silica phase, only the AT phases are compared to each other.

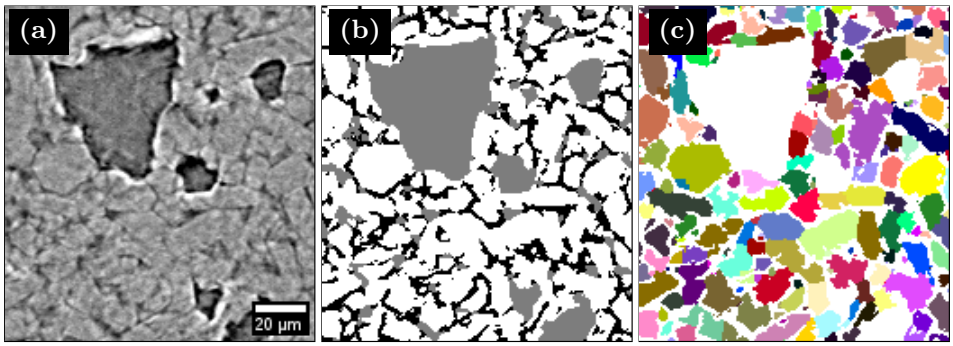


FIGURE 9. 2D cutout of an SXCT image for the "flexible" scenario AT-F (a), its phase-wise (b) and grain-wise (c) segmentation.

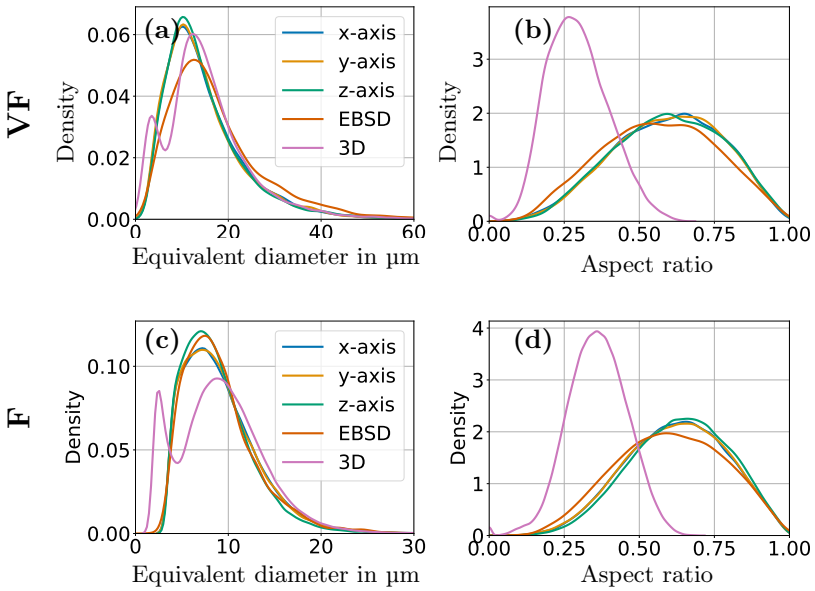


FIGURE 10. Probability densities of equivalent diameters (left column) and aspect ratios (right column). Different colors are indicating virtual cross sections of the 3D image derived by SXCT along different axes, as well as the 2D EBSD measurements. The pink curve indicates the probability densities corresponding to (volume-based) equivalent diameter and aspect ratio determined from 3D image data. The upper row corresponds to the AT-VF scenario, whereas the lower row corresponds to AT-F. Note that the x-axes of (a) and (c) are scaled differently.

Figures 10a and 10b present a comparison of the probabilities densities of the area-equivalent diameter and aspect ratio derived by SXCT and EBSD for the VF scenario. The area-equivalent diameters exhibit similar probability densities for virtual cross sections along the three coordinate axes, confirming spatial homogeneity, as mentioned in the previous sections. Furthermore, the area-equivalent diameters derived from the EBSD measurements show qualitatively similar behavior. However, grains measured with EBSD tend to be slightly larger. In fact, EBSD allows for a better definition of the grain boundaries, thanks to its high spatial resolution. In addition, the probability densities of the aspect ratio, see Figure 10b, show no significant differences between the grains measured by SXCT and EBSD, respectively. Note that the good agreement between the virtual and EBSD cross sections can be considered as validation of the 3D segmentation of SXCT images, based on iterative morphological reconstruction.

When comparing the probability densities of area-equivalent diameters derived from (virtual) 2D cross sections with those of volume-equivalent diameters derived from the complete 3D image, significant differences appear due to stereological effects. In Figure 10a, the curve corresponding to the volume-equivalent diameter exhibits two peaks, representing the two grain populations discussed in Section 3.2. In contrast, the four curves corresponding to area-equivalent diameter determined from 2D cross sections show a unimodal distribution. This discrepancy can be explained by two effects. Firstly, the probability of intersecting a grain by a random plane is proportional to its size [53], making smaller grains less likely to appear in (experimental or virtual) cross sections. Secondly, since grains are generally not intersected through their centers, cross sections appear smaller than the actual size of the grain. These two effects may lead to a smooth and unimodal distribution of area-equivalent diameters derived from 2D cross sections.

Furthermore, the aspect ratios (see Figure 10b) determined from 3D grains tend to be smaller, implying more elongated grains. This aspect ratio represents the minimum aspect ratio, which would be observable in a 2D cross section. It would correspond to a cross section that would be perpendicular to the $a_1-a_3-$plane of the grain (and goes through its center). As in Section 2.5.1, $a_1, a_2, a_3$ indicate the direction of the major, intermediate, and minor axes of a grain. Conversely, if the cross section is perpendicular to the $a_2 - a_3-$plane, the maximum in the observable 2D aspect ratio would be obtained, which in the present paper is approximately equal to one, since $\ell_2 \approx \ell_3$, see Figure 7d. Since the cross sections can be considered random, the grain cross sections are realized between these two extreme scenarios, corresponding to aspect ratios within this range.

Figures 10c and 10d show probability densities of equivalent diameters and aspect ratios corresponding to the F scenario. Analogously to the VF scenario, the curves corresponding to both the equivalent diameter and the aspect ratio, derived from virtual cross sections along different directions, are matching and show a similar behavior compared to the curves obtained from the 2D EBSD image. Furthermore, the discrepancies between 2D- and 3D-based descriptors show the same behavior as in the VF case and can be explained with the same arguments.

It is interesting to note that the 2D-based aspect ratios of the F and VF materials exhibit a similar behavior, although the 3D-based aspect ratios for the VF scenario tend to be smaller than those observed for the F material. This suggests that quantifying the degree of grain elongation based solely on 2D cross sections is a challenging task.

## 4. Conclusion

Through the use of advanced statistical methods, microstructural 2D EBSD and 3D SXCT data of aluminum titanate (AT) refractory materials were analyzed and various geometric descriptors were determined.

In particular, a novel object-wise segmentation algorithm was developed that is capable of segmenting strongly elongated grains. It is based on an iterative application of morphological reconstruction combined with a watershed transform. The performance of this advanced algorithm is validated by comparing virtual 2D cross sections of 3D SXCT data to experimental ones derived from 2D EBSD measurements. For a comprehensive performance evaluation against other segmentation methods, benchmark tests are required within a set-up where the ground true segmentation is known. Furthermore, the presented algorithm can be generalized to other applications by adapting the criterion to accept correctly segmented objects. For example, the convexity used in this paper could be replaced by an aspect ratio-based criterion.

Following the segmentation of individual pores and AT grains, various size, shape and further geometric descriptors were determined. These revealed two populations of pores and grains, which differ in their morphological properties. The properties of these populations are correlated with the mechanisms of diffusion and grain growth, as well as pore coalescence, during sintering. In particular, large, irregular-shaped pores may stem from poor powder compaction, while small pores may emerge during sintering. Furthermore, a correlation between the spatial orientation of grains and the presence and size of pores is observed. Small pores may promote grain growth, while large pores tend to inhibit it.

Finally, descriptors derived from 2D EBSD data are compared to those from virtual 2D cross section extracted from 3D SXCT image data. Strong agreement of these two types of descriptors is observed, which offers insight in the complementary information on the morphology of such materials derived by both imaging techniques.

## Acknowledgement

This study was carried out in the framework of the international research project HoTMiX (Micromechanical behavior of nanostructured oxides at very high temperatures) co-funded by the French National Research Agency (ANR) (Grant No. ANR 19 CE09 0035) and Deutsche Forschungsgemeinschaft (DFG) (Grant No. DFG 431178689).

## Data availability

The datasets generated during and/or analyzed during the current study are available from the corresponding authors on reasonable request.

## References

[1] Y. Aoki, H. Yoshida, H. Masuda, and E. Tochigi. Overcoming the intrinsic brittleness of high-strength $Al_2O_3$-$GdAlO_3$ ceramics through refined eutectic microstructure. *Nature Communictaions*, 15:8700, 2024.

[2] I. Kim and L. Gauckler. Formation, decomposition and thermal stability of $Al_2TiO_5$ ceramics. *Journal of Ceramic Science and Technology*, 3:49–60, 2012.

[3] W. Chen, A. Shui, Q. Shan, J. Lian, C. Wang, and J. Li. The influence of different additives on microstructure and mechanical properties of aluminum titanate ceramics. *Ceramics International*, 47:1169–1176, 2021.

[4] G. Bruno, Y. Kilali, and A. M. Efremov. Impact of the non-linear character of the compressive stress–strain curves on thermal and mechanical properties of porous microcracked ceramics. *Journal of the European Ceramic Society*, 33:211–219, 2013.

[5] S. B. Ogunwumi. Strontium feldspar aluminium titanate for high temperature applications. *Patent No. US6620751B1. Corning Inc.*, 2003.

[6] S. Das. The Al-O-Ti (aluminum-oxygen-titanium) system. *Journal of Phase Equilibria*, 23:525–536, 2002.

[7] K. Kornaus, P. Rutkowski, R. Lach, and A. Gubernat. Effect of microstructure on thermal and mechanical properties of solid solutions $Al_2TiO_5$ - $MgTi_2O_5$. *Journal of the European Ceramic Society*, 41:1498–1505, 2021.

[8] M. Ilatovskaia, G. Savinykh, and O. Fabrichnaya. Thermodynamic description of the Ti-Al-O system based on experimental data. *Journal of Phase Equilibria and Diffusion*, 38: 175–184, 2017.

[9] Y. Ohya, S. Yamamoto, T. Ban, M. Tanaka, and S. Kitaoka. Thermal expansion and mechanical properties of self-reinforced aluminum titanate ceramics with elongated grains. *Journal of the European Ceramic Society*, 37:1673–1680, 2017.

[10] G. Bayer. Thermal expansion characteristics and stability of pseudobrookite-type compounds, $Me_3O_5$. *Journal of the Less Common Metals*, 24:129–138, 1971.

[11] D. Hasselman. Unified theory of thermal shock facture initiation and crack propagation in brittle ceramics. *Journal of the American Ceramic Society*, 52:600–604, 2006.

[12] M. Mouiya, D. Tingaud, Y. Tamraoui, E. Thune, N. Tessier-Doyen, R. Guinebretière, J. Alami, and M. Huger. Crystallography and anisotropy of crystals shape in dense aluminum titanate ceramics. *Journal of the European Ceramic Society*, 44:4761–4771, 2024.

[13] P. Withers, C. Bouman, S. Carmignato, V. Cnudde, D. Grimaldi, C. Hagen, E. Maire, M. Manley, A. Du Plessis, and S. Stock. X-ray computed tomography. *Nature Reviews Methods Primers*, 1:18, 2021.

[14] S. Stock. *Developments in X-ray Tomography VII*. SPIE, 2010.

[15] Ö. Çiçek, A. Abdulkadir, S. S. Lienkamp, T. Brox, and O. Ronneberger. 3D U-Net: Learning dense volumetric segmentation from sparse annotation. In *Proceedings of the Medical Image Computing and Computer-Assisted Intervention, Athens, Greece*, pages 424–432. Springer, 2016.

[16] O. Furat, T. Kirstein, T. Leißner, K. Bachmann, J. Gutzmer, U. A. Peuker, and V. Schmidt. Multidimensional characterization of particle morphology and mineralogical composition using CT data and R-vine copulas. *Minerals Engineering*, 206:108520, 2024.

[17] S. Weber, O. Furat, T. Kirstein, T. Leißner, U. A. Peuker, and V. Schmidt. Computational workflow for the characterization of size, shape, and composition of particles and their separation behavior during processing. *Powders*, 4:1, 2025.

[18] A. Spettl, R. Wimmer, T. Werz, M. Heinze, S. Odenbach, C. E. Krill, and V. Schmidt. Stochastic 3D modeling of Ostwald ripening at ultra-high volume fractions of the coarsening phase. *Modelling and Simulation in Materials Science and Engineering*, 23:065001, 2015.

[19] B. Prifling, A. Ridder, A. Hilger, M. Osenberg, I. Manke, K. P. Birke, and V. Schmidt. Analysis of structural and functional aging of electrodes in lithium-ion batteries during rapid charge and discharge rates using synchrotron tomography. *Journal of Power Sources*, 443:227259, 2019.

[20] L. Vincent. Morphological grayscale reconstruction in image analysis: Applications and efficient algorithms. *IEEE Transactions on Image Processing*, 2:176–201, 1993.

[21] A. Ridder, B. Prifling, A. Hilger, M. Osenberg, M. Weber, I. Manke, K. P. Birke, and V. Schmidt. Quantitative analysis of cyclic aging of lithium-ion batteries using synchrotron tomography and electrochemical impedance spectroscopy. *Electrochimica Acta*, 444:142003, 2023.

[22] M. Mouiya, N. Tessier-Doyen, Y. Tamraoui, J. Alami, and M. Huger. High temperature thermomechanical properties of a microcracked model refractory material: A silica-doped aluminium titanate. *Ceramics International*, 49:24572–24580, 2023.

[23] M. Mouiya, M. Martynyuk, A. Kupsch, R. Laquai, B. Müller, N. Tessier-Doyen, Y. Tamraoui, I. Serrano-Munoz, M. Huger, M. Kachanov, and G. Bruno. The stress–strain behavior of refractory microcracked aluminum titanate: The effect of zigzag microcracks and its modeling. *Journal of the American Ceramic Society*, 106:6995–7008, 2023.

[24] A. Doncieux, D. Stagnol, M. Huger, T. Chotard, C. Gault, T. Ota, and S. Hashimoto. Thermo-elastic behaviour of a natural quartzite: itacolumite. *Journal of Materials Science*, 43:4167–4174, 2008.

[25] A. Rack, S. Zabler, B. Müller, H. Riesemeier, G. Weidemann, A. Lange, J. Goebbels, M. Hentschel, and W. Görner. High resolution synchrotron-based radiography and tomography using hard X-rays at the BAMline (BESSY II). *Nuclear Instruments and Methods in Physics Research Section A: Accelerators, Spectrometers, Detectors and Associated Equipment*, 586:327–344, 2008.

[26] H. Markötter, M. Sintschuk, R. Britzke, S. Dayani, and G. Bruno. Upgraded imaging capabilities at the BAMline (BESSY II). *Journal of Synchrotron Radiation*, 29:1292–1298, 2022.

[27] H. Markötter, B. Müller, A. Kupsch, S. Evsevleev, T. Arlt, A. Ulbricht, S. Dayani, and G. Bruno. A review of X-ray imaging at the BAMline (BESSY II). *Advanced Engineering Materials*, 25:2201034, 2023.

[28] D. Gursoy, F. Carlo, X. Xiao, and C. Jacobsen. TomoPy: a framework for the analysis of synchrotron tomographic data. *Journal of Synchrotron Radiation*, 21:1188–1193, 2014.

[29] F. Marone and M. Stampanoni. Regridding reconstruction algorithm for real-time tomographic imaging. *Journal of Synchrotron Radiation*, 19:1029–1037, 2012.

[30] S. Van der Walt, J. L. Schönberger, J. Nunez-Iglesias, F. Boulogne, J. D. Warner, N. Yager, E. Gouillart, and T. Yu. scikit-image: Image processing in Python. *PeerJ*, 2:e453, 2014.

[31] F. Bachmann, R. Hielscher, and H. Schaeben. Grain detection from 2D and 3D EBSD data - specification of the MTEX algorithm. *Ultramicroscopy*, 111:1720–1733, 2011.

[32] The MathWorks Inc. Matlab, 2024. Version: 24.1.0.2568132 (R2024a).

[33] P. Soille. *Morphological Image Analysis: Principles and Applications*. Springer, 1999.

[34] Comet Technologies Canada Inc. Dragonfly, 2024. Version: 2024.1.

[35] J. Russ. *The Image Processing Handbook*. CRC Press, 5th edition, 2006.

[36] R. C. Gonzalez and R. E. Woods. *Digital Image Processing*. Prentice Hall, 2008.

[37] S. Beucher and F. Meyer. The morphological approach to segmentation: The watershed transformation. In E. R. Dougherty, editor, *Mathematical Morphology in Image Processing*, page 433–481. Marcel Dekker Inc, 1993.

[38] J. Roerdink and A. Meijster. The watershed transform: Definitions, algorithms and parallelization strategies. *Fundamenta Informaticae*, 41:187–228, 2000.

[39] J. Zheng and R. D. Hryciw. Segmentation of contacting soil particles in images by modified watershed analysis. *Computers and Geotechnics*, 73:142–152, 2016.

[40] R. Sekerka. Equilibrium and growth shapes of crystals: How do they differ and why should we care? *Crystal Research and Technology*, 40:291 – 306, 2005.

[41] P. Rieder, L. Petrich, I. Serrano-Munoz, R. Fernández, G. Bruno, and V. Schmidt. Statistical comparison of substructures in pure aluminum before and after creep deformation, based on EBSD image data. *Microscopy and Microanalysis*, 29:1889–1900, 2023.

[42] T. Hastie, R. Tibshirani, and J. Friedman. *The Elements of Statistical Learning: Data Mining, Inference, and Prediction*. Springer, 2009.

[43] J. Ohser and K. Schladitz. *3D Images of Materials Structures*. Wiley-VCH, 2009.

[44] P. Virtanen, R. Gommers, T. E. Oliphant, M. Haberland, T. Reddy, D. Cournapeau, E. Burovski, P. Peterson, W. Weckesser, J. Bright, S. J. van der Walt, M. Brett, J. Wilson, K. J. Millman, N. Mayorov, A. R. J. Nelson, E. Jones, R. Kern, E. Larson, C. J. Carey, İ. Polat, Y. Feng, E. W. Moore, J. VanderPlas, D. Laxalde, J. Perktold, R. Cimrman, I. Henriksen, E. A. Quintero, C. R. Harris, A. M. Archibald, A. H. Ribeiro, F. Pedregosa, P. van Mulbregt, and SciPy 1.0 Contributors. SciPy 1.0: Fundamental Algorithms for Scientific Computing in Python. *Nature Methods*, 17:261–272, 2020.

[45] D. W. Scott. *Multivariate Density Estimation: Theory, Practice, and Visualization*. J. Wiley & Sons, 2nd edition, 2015.

[46] T.-T. Fang and H. Palmour III. Evolution of pore morphology in sintering powder compacts. *Ceramics International*, 16:1–10, 1990.

[47] R. Brook. Pore-grain boundary interaction and grain growth. *Journal of the American Ceramic Society*, 52:56 – 57, 1969.

[48] J. Zhao and M. Harmer. Effect of pore distribution on microstructure development: II, first- and second-generation pores. *Journal of the American Ceramic Society*, 71:530 – 539, 1988.

[49] Y. Onel, A. Lange, A. Staude, K. Ehrig, A. Kupsch, M. Hentschel, T. Wolk, B. Müller, and G. Bruno. Evaluating porosity in cordierite diesel particulate filter materials, Part 2. Statistical analysis of computed tomography data. *Journal of Ceramic Science and Technology*, 5:13–22, 2014.

[50] C. Chen, B. R. Müller, C. Prinz, J. Stroh, I. Feldmann, and G. Bruno. The correlation between porosity characteristics and the crystallographic texture in extruded stabilized aluminium titanate for diesel particulate filter applications. *Journal of the European Ceramic Society*, 40:1592–1601, 2020.

[51] C. H. Wörner and P. M. Hazzledine. Grain growth stagnation by inclusions or pores. *Journal of the Minerals, Metals & Materials Society (JOM)*, 44:16–20, 1992.

[52] D. Gouvêa. Thermodynamic of solid-state sintering: Contributions of grain boundary energy. *Journal of the European Ceramic Society*, 44:116677, 2024.

[53] A. Baddeley and E. Jensen. *Stereology for Statisticians*. Taylor & Francis, 2004.